PAPER • OPEN ACCESS

Atomic-scale study of type-II Dirac semimetal PtTe$_2$ surface

To cite this article: Pablo Casado Aguilar *et al* 2022 *J. Phys. Mater.* **5** 044003

View the article online for updates and enhancements.

Journal of Physics: Materials

CrossMark

PAPER

Atomic-scale study of type-II Dirac semimetal PtTe$_2$ surface

Pablo Casado Aguilar[1,2], Fabian Calleja[1], Chia-Nung Kuo[3], Chin Shan Lue[3], Barun Ghosh[4], Amit Agarwal[4], Antonio Politano[5] (iD), Amadeo L Vázquez de Parga[1,2,6,7], Rodolfo Miranda[1,2,6,7], Jose Angel Silva-Guillén[1] (iD) and Manuela Garnica[1,6,*] (iD)

1 Instituto Madrileño de Estudios Avanzados en Nanociencia (IMDEA-Nanociencia), 28049 Madrid, Spain
2 Departamento de Física de la Materia Condensada, Universidad Autónoma de Madrid, 28049 Madrid, Spain
3 Department of Physics, National Cheng Kung University, 70101 Tainan, Taiwan
4 Department of Physics, Indian Institute of Technology Kanpur, 208016 Kanpur, India
5 Dipartimento di Scienze Fisiche e Chimiche (DSFC), Università degli Studi dell'Aquila, I-67100 L'Aquila, Italy
6 Instituto 'Nicolás Cabrera', Universidad Autónoma de Madrid, 28049 Madrid, Spain
7 Condensed Matter Physics Center (IFIMAC), Universidad Autónoma de Madrid, 28049 Madrid, Spain
* Author to whom any correspondence should be addressed.

E-mail: manuela.garnica@imdea.org

Abstract

Dirac semimetals (DSM) host linear bulk bands and topologically protected surface states, giving rise to exotic and robust properties. Platinum ditelluride (PtTe$_2$) belongs to this interesting group of topological materials. Here, we employ scanning tunneling microscopy (STM) in combination with first-principles calculations to visualize and identify the native defects at the surface of a freshly cleaved PtTe$_2$ crystal. Around these defects, short-wavelength electron density oscillations are observed. Fourier transform analysis of the energy-dependent quasiparticle interference patterns is in good agreement with our calculated joint density of states, demonstrating the singular properties of the surface of this type-II DSM. Our results evidence the power of STM in understanding the surface of topological materials.

1. Introduction

In Dirac semimetals (DSM), doubly degenerate conduction and valence bands touch at discrete points, the so-called Dirac nodes, around which the energy dispersion is linear. The ordinary electrons in these materials mimic the behavior of massless Dirac fermions in analogy to two dimensional materials, i.e. graphene, or the surface states (SS) of a topological insulator. Accordingly, DSM have recently attracted considerable interest because they can serve as platforms for studying the physics of Dirac fermion systems. Interestingly, DSM possess topologically protected SS with important implications in their magnetization and transport properties, such as the chiral anomaly effect [1, 2] or large magnetoresistance [3, 4].

To date, many materials have been identified as DSM, such as Na$_3$Bi [2, 5], Cd$_3$As$_2$ [3, 4, 6–10], and ZrTe$_5$ [11]. In addition, transition metal dichalcogenides (TMDs), i.e. PtSe$_2$, PdTe$_2$, NiTe$_2$ and PtTe$_2$, have been recently predicted to be type-II DSM [12, 13], where the linear dispersion is tilted and the Dirac points appear at the band touching points of electron and hole pockets. Evidences of strongly tilted Dirac cones and closed Fermi surfaces were confirmed in these systems by angle-resolved photoemission spectroscopy [14–20] and transport measurements [21–23]. Complementary, scanning tunneling microscopy (STM) enables the direct visualization of their surface structure including native defects [24–28]. Typical native defects in TMDs are vacancies, interstitial impurities and substitutional impurities. The role of the native defects in the electronic and topological properties of the materials was demonstrated to be crucial, causing layer-dependent magnetism [29], tailoring surface chemical reactivity [30] or reducing the magnetic gap in an antiferromagnetic topological insulator [31], among others. Consequently, in order to improve the quality of DSM crystals for their future implementation in electronic devices, the identification of defects is

fundamental to understand the role they play in their electronic properties. In addition, STM can be used to directly probe SS through the study of the local oscillations produced by their scattering with defects, adatoms and steps [32, 33]. The analysis of the fast Fourier transform of the local density of states (LDOS) maps given by the spatial distribution of differential conductance measured by STM will provide quantitative information about the band structure and SS. The connection between LDOS maps and k-space spectral information is achieved through the calculation of the joint density of states (JDOS). However, type-II DSM have not been yet characterized by this technique.

Here, we present a surface investigation of a trigonal (1T)-PtTe$_2$ crystal by means of high-resolution STM combined with first-principles calculations. We find four different types of native defects after cleaving the crystal in ultra-high vacuum (UHV). By comparing the experimental and simulated STM images, we are able to identify each of these defects. The type and density of defects that we observe, differ from a previous study on the same material [27]. This discrepancy is mainly related to the different growth process between the studied crystals, highlighting the importance of carefully controlling the Pt:Te ratio during the synthesis process. The elastic scattering of the surface electrons by point or extended defects mixes eigenstates with different k vectors, but located on the same quasiparticle constant energy contour (CEC) in k-space. This gives rise to an interference pattern known as quasiparticle interference (QPI) map. The Fourier analysis of our experimental QPI maps at a given bias voltage gives us the q vectors connecting the different points on the corresponding CEC at that energy and are in good agreement with the simulated JDOS, confirming the presence of a Dirac cone and two SS in the 1T-PtTe$_2$ crystal.

2. Methods

1T-PtTe$_2$ crystals were grown by the self-flux method, as described in [34]. The crystal was introduced in a UHV chamber, cleaved by scotch tape and directly transferred to a low-temperature STM. The base pressure during this procedure was 8×10^{-10} mbar. STM measurements were performed in a custom-designed UHV chamber equipped with a low temperature STM working at either 1.2 K or 4.2 K. All STM images were taken in constant-current mode and the differential conductance (dI/dV) spectra were taken using a lock-in amplifier ($f = 763$ Hz, $V_{pp} = 50$ mV). STM data were processed with the WSxM software [35]. The Fourier transforms of the QPI maps have been symmetrized to improve the signal to noise ratio (see supplementary material (SM) for more information).
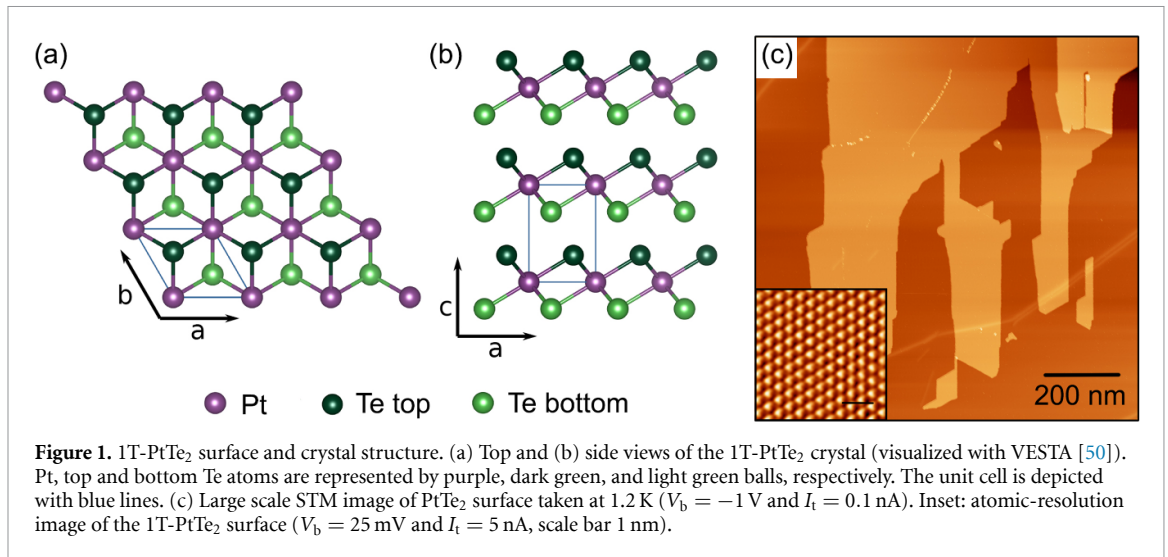
First-principles calculations were carried out within the density functional approach as implemented in QuantumEspresso [36–38]. We used the generalized gradient approximation and, in particular, the Perdew–Burke–Ernzerhof (PBE) functional [39]. Only the valence electrons were considered in the calculation, with the core being replaced by ultrasoft full relativistic pseudopotentials including nonlinear core-corrections [40]. The energy cutoff for the wave functions and the charge density were set to 150 Ry and 750 Ry, respectively. The Brillouin zone (BZ) was sampled with the Monkhorst–Pack scheme [41] using a ($12 \times 12 \times 6$) grid. To perform the surface calculations, we built a tight-binding Hamiltonian using maximally localized Wannier functions as implemented in Wannier90 [42] with p and d orbitals. We then calculated the surface state spectrum and the JDOS as implemented in the code wanniertools [43], in which we used a system containing 20 layers to correctly reproduce the bulk states. The JDOS can be calculated as [43–45]:

$$\mathrm{JDOS}(\mathbf{q}, \epsilon) = \frac{1}{2} \sum_{\mathbf{k}} \rho(\mathbf{k}, \epsilon)\rho(\mathbf{k}+\mathbf{q}, \epsilon), \tag{1}$$

where $\rho(\mathbf{k}, \epsilon) = -\frac{1}{\pi}\mathbb{Im}\{\mathrm{Tr}[G(\mathbf{k}, \epsilon)]\}$. The last term is the Green's function at the k-point $\mathbf{k}$ and energy ϵ. Finally, STM simulations were performed within the Tersoff–Hamann approximation, as implemented in Siesta [46, 47]. In order to make the calculations consistent between the two codes, we used PBE for the exchange-correlation functional. The energy cutoff of the real space integration mesh was set to 500 Ry. We built two different supercells of a bilayer of PtTe$_2$ to simulate the defects, i.e. (8×8) and (14×14). The BZ was sampled with the Monkhorst–Pack scheme [41] using grids of ($5 \times 5 \times 1$) and ($1 \times 1 \times 1$), respectively. Unless stated otherwise, the experimental crystal structure determined by x-ray diffraction (XRD) was adopted for the calculations [34, 48].

3. Structural characterization

Top and side views of the crystal structure of bulk PtTe$_2$ are displayed in figures 1(a) and (b), respectively. PtTe$_2$ crystallizes in the CdI$_2$-type 1T structure with $P\bar{3}m1$ space group. The high crystalline quality is confirmed by XRD [34] and STM topographic images. Figure 1(c) shows a large scale STM image of the PtTe$_2$ surface after *in-situ* cleavage. Large terraces of the order of hundreds of nanometers are resolved and

Figure 1. 1T-PtTe$_2$ surface and crystal structure. (a) Top and (b) side views of the 1T-PtTe$_2$ crystal (visualized with VESTA [50]). Pt, top and bottom Te atoms are represented by purple, dark green, and light green balls, respectively. The unit cell is depicted with blue lines. (c) Large scale STM image of PtTe$_2$ surface taken at 1.2 K ($V_b = -1$ V and $I_t = 0.1$ nA). Inset: atomic-resolution image of the 1T-PtTe$_2$ surface ($V_b = 25$ mV and $I_t = 5$ nA, scale bar 1 nm).
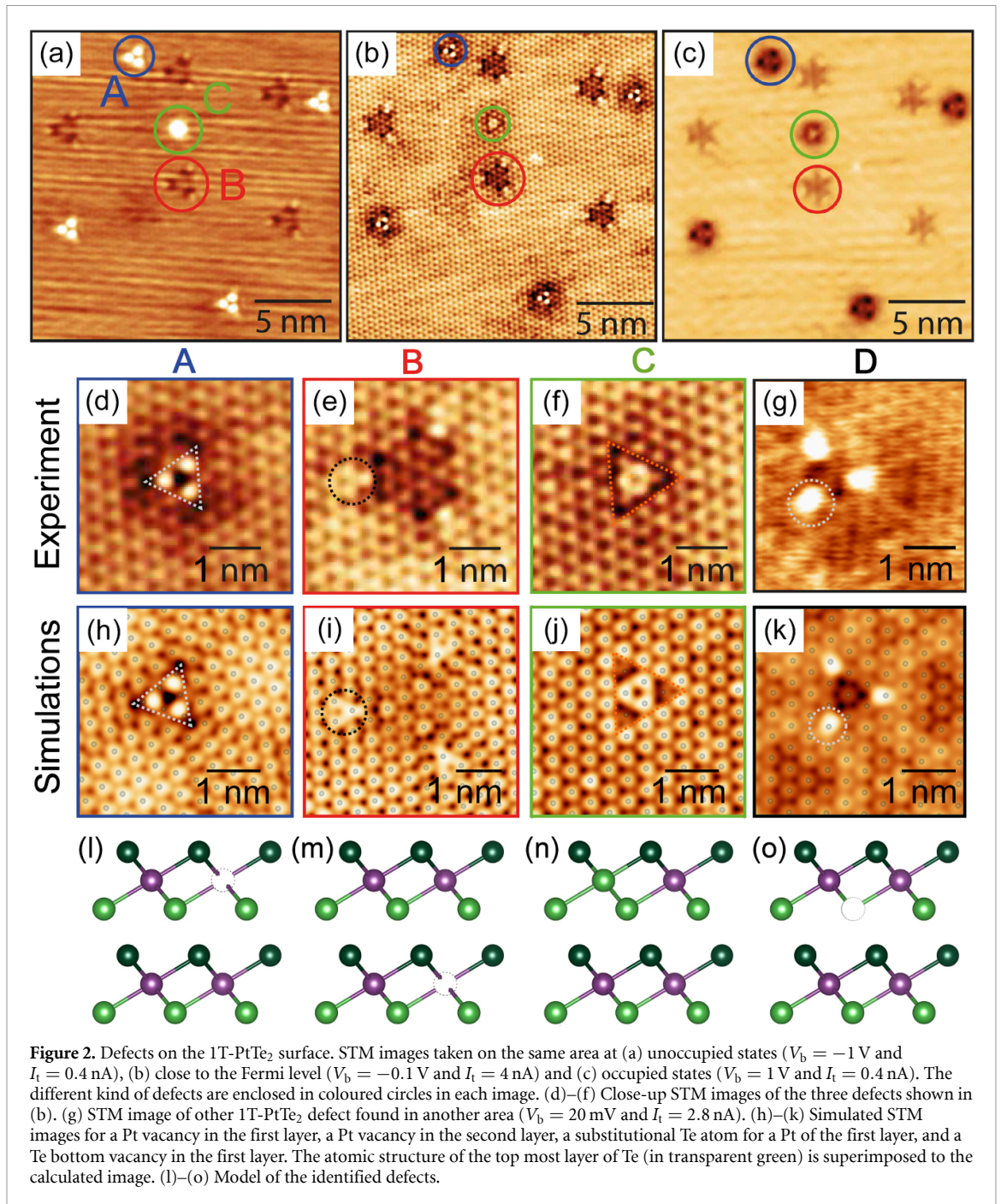
the measured step height is 4.9 ± 0.3 Å, which matches closely the bulk value of $c = 5.19$ Å measured by XRD [34, 48]. This is an indication of single-layer steps. A typical atomic-resolution STM image is shown as an inset in figure 1(c). The lattice constant measured is $a = (3.8 \pm 0.3)$ Å consistent with previous results [48, 49] and helium and XRD measurements [34, 48].
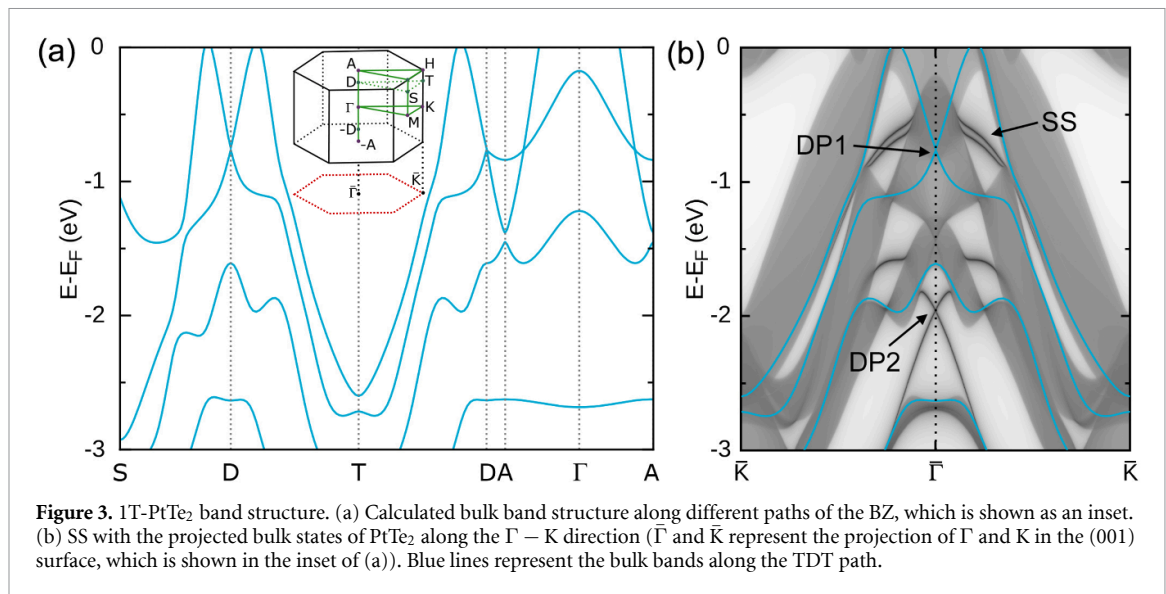
High-resolution STM images of the PtTe$_2$ surface reveal the presence of randomly distributed native defects with different aspect as a function of the bias voltage. Figure 2 shows the same area taken at three distinct tunneling parameters where three native defects are resolved, labeled as A (blue circle), B (red circle) and C (green circle). For unoccupied states (figure 2(a)), defects A and C look as bright protrusions with different symmetry, while defect B appears as a dark triangle surrounded by bright regions. For occupied states (figure 2(c)) all of them look dark. STM images taken close to the Fermi level, figure 2(b), allow visualizing the atomic lattice of the first Te layer, concurrently with the defects.

As a first step towards their identification, we performed a detailed analysis of each type of defect and a study of their density. The most common defect in our samples is the type A (figure 2(d)) with a density of 7.23×10^{11} cm^{-2}. It presents a three-fold symmetry composed by three bright protrusions matching the in-plane lattice parameter of the first Te layer (figure 2(b)). Similar defects were previously reported in other transition metal chalcogenides (TMCs), i.e. PtSe$_2$ [26], NiTe$_2$ [24] and MnBi$_2$Te$_4$ [31], and attributed to vacancies or chalcogen substitutions in the first metallic layer of the TMCs. The second most frequently observed defect is the type B (figure 2(e)), with an incidence of 6.90×10^{11} cm^{-2}. Its size is larger as compared to type A and it extends along six in-plane lattice parameters, indicating that it is located in a deeper layer than defect A. In addition, a third kind of defect can be resolved in figure 2(a) with a lower density of 1.90×10^{11} cm^{-2}. This defect, labeled as type C, changes drastically its appearance as a function of the sample voltage, showing up as a bright protrusion at unoccupied states and a dark ring at occupied states. Finally, an additional defect (figure 2(g)) is also found although much less abundant, type D. Surprisingly, we did not observe Te vacancies, in contrast to previous works on PtTe$_2$ crystals [27] and other TMDs [24, 51] where they are resolved as depressions at Te-terminated surfaces. We attribute this to the different growth process used in our work. Our PtTe$_2$ crystals were grown by the self-flux technique instead of electronic deposition [27]. The high Te ratio during the process is probably responsible of the formation of the different atomic defects.

To get a deeper insight into the nature of the observed point defects, we have performed STM simulations (see section 2) for all possible defects located in the first and second layers and we compared them with our experimental findings. These calculations were performed using $a = 4.01$ Å and $c = 5.06$ Å. Although previous measurements and calcultions were reported for parental compounds [24–27, 52], a clear identification of the defects is still lacking. Interestingly, by performing a large number of simulations for different defects and comparing them with the STM measurements, we can unequivocally identify the defects present in PtTe$_2$. Figures 2(h)–(k) show the simulated STM images of four different defects. We assign the type A defect to a single vacancy of Pt in the topmost trilayer of PtTe$_2$, figures 2(h) and (l). The three-fold symmetric shape observed in the STM measurements (see grey triangle in figure 2(d)) is well reproduced by simulations (figure 2(h)). In particular, we reproduce the three bright lobes forming a triangle surrounded by a dark spot at the vertices of the highlighted grey triangle. The second most abundant defect, type B, can be identified as a Pt vacancy in the second trilayer (figures 2(i) and (m)). We base our assignment in the good

Figure 2. Defects on the 1T-PtTe$_2$ surface. STM images taken on the same area at (a) unoccupied states ($V_b = -1$ V and $I_t = 0.4$ nA), (b) close to the Fermi level ($V_b = -0.1$ V and $I_t = 4$ nA) and (c) occupied states ($V_b = 1$ V and $I_t = 0.4$ nA). The different kind of defects are enclosed in coloured circles in each image. (d)–(f) Close-up STM images of the three defects shown in (b). (g) STM image of other 1T-PtTe$_2$ defect found in another area ($V_b = 20$ mV and $I_t = 2.8$ nA). (h)–(k) Simulated STM images for a Pt vacancy in the first layer, a Pt vacancy in the second layer, a substitutional Te atom for a Pt of the first layer, and a Te bottom vacancy in the first layer. The atomic structure of the top most layer of Te (in transparent green) is superimposed to the calculated image. (l)–(o) Model of the identified defects.

matching between simulation and experiment, and the similar incidence of this defect with respect to the Pt vacancy in the first layer. This defect is slightly more extended spatially, as expected for a deeper defect, and displays three brighter Te atoms at the corner of a darker region, marked with a black dashed circle in figure 2(e) and (i). We can ascribe type C defects with an antisite substitution of a Pt atom in the first trilayer by a Te atom, see figures 2(j) and (n). In this defect, a darker triangular shape with three lobes at the center exists. As before, the simulation nicely reproduces the observed features. In particular, we can reproduce the dark region (marked with an orange triangle in figure 2(j)), inside of which three bright Te atoms can be resolved. Finally, we associated the least abundant defect, type D, with a Te bottom vacancy in the topmost trilayer of PtTe$_2$ (figures 2(k) and (o)). Both experimental and simulated images of this defect show a dark central region enclosed by three bright, rectangularly-shaped spots (grey circle in figure 2(g) and (k)). These spots are more extended than the spots observed in the other defects, as clearly captured in the simulation. Remarkably, not only the simulations and experiment agree at energies close to the Fermi level, but the similarity between them also holds for the measurements performed at +1 V and −1 V, (see figure S5 in the SM). It is important to note that we have also simulated a large number of different defects, see figure S6 in the SM, and we have found that the defects shown in this section are those that better fit the experimental

Figure 3. 1T-PtTe$_2$ band structure. (a) Calculated bulk band structure along different paths of the BZ, which is shown as an inset. (b) SS with the projected bulk states of PtTe$_2$ along the $\Gamma - K$ direction ($\bar{\Gamma}$ and $\bar{K}$ represent the projection of Γ and K in the (001) surface, which is shown in the inset of (a)). Blue lines represent the bulk bands along the TDT path.
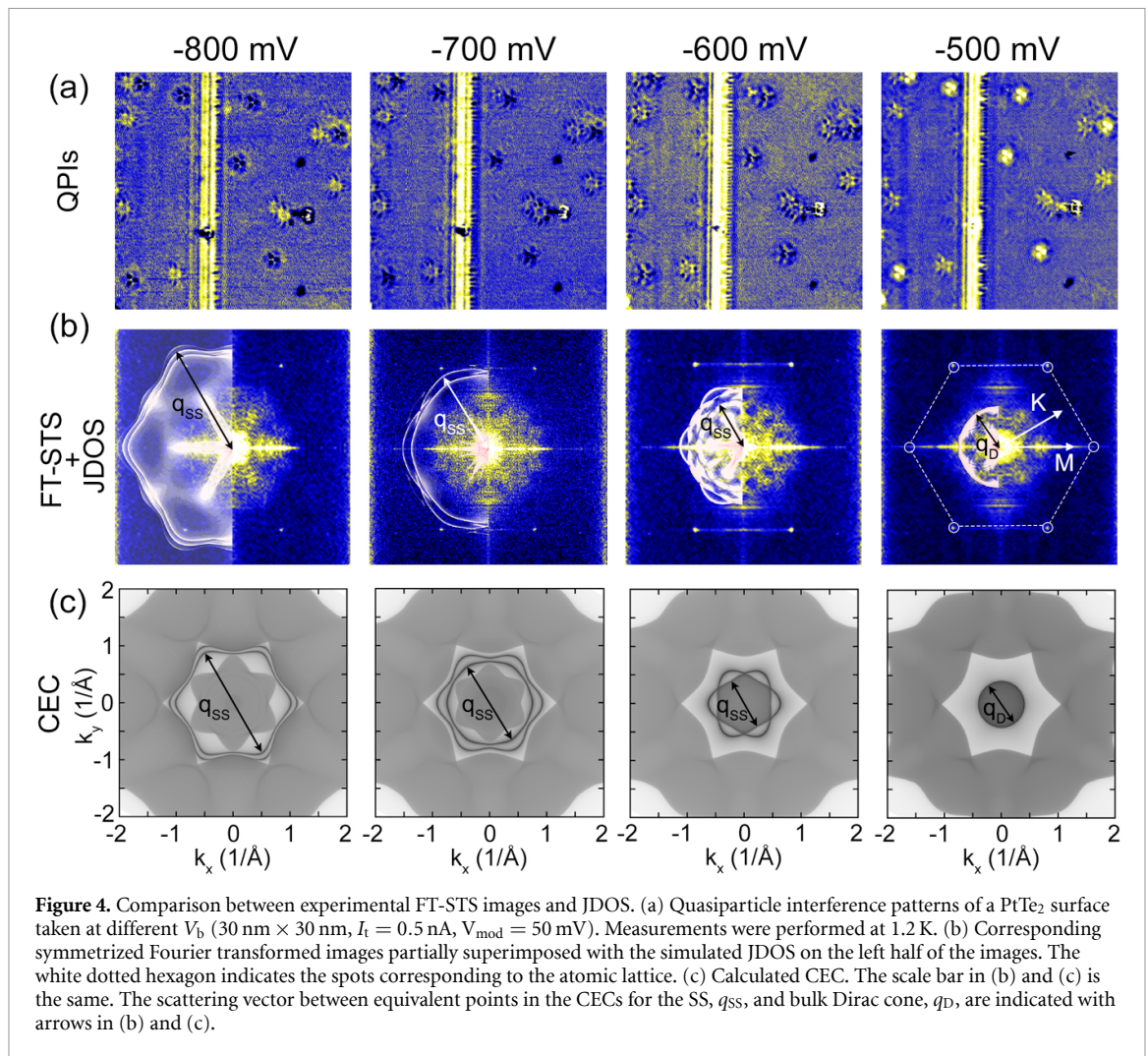
features. Due to the large number of defects simulated and based in the incidence of each defect, we can unambiguously confirm the identification of the experimental defects.

4. Electronic properties

In figure 3(a), the calculated band structure of the bulk PtTe$_2$ along different paths of the BZ is reported. In addition, we calculated the spectral function of PtTe$_2$, on which the bulk bands are superimposed (figure 3(b)). Interestingly, two main features can be resolved at the $\bar{\Gamma}$ point. First, there is a conical dispersion around -0.8 eV, marked as DP1, due to the continuous bulk states. Moreover, two SS emerge out around the Dirac cone, labeled as SS. Second, a surface Dirac cone is located at -2.0 eV. This arises from a bulk band inversion in the Te-p orbital manifold along the $\Gamma - A$ direction. These features are well reproduced by our STS measurements, see figure S1 of SM and [34].

To probe the unique electronic structure of the 1T-PtTe$_2$, we acquired differential conductance, dI/dV, maps at different sample voltages in a 30 nm $\times$ 30 nm area with a trench and several point defects. Figures 4(a) and (b) show the QPI maps and their corresponding symmetrized Fourier transformed scanning tunneling spectroscopy (FT-STS) images. The topographic STM image in this area is shown in figure S2 of the SM. The QPI maps from -500 mV to -800 mV show weak, incommensurate, spatial modulations in the tunneling conductance, i.e. short-wavelength oscillations of LDOS around defects, which change with bias voltage. The dispersion of their wavevectors with energy is reflected in the corresponding FT-STS images at different energies. In addition to the relevant scattering wavevectors, q, the six-fold periodic lattice of the 1T-PtTe$_2$ crystal is always resolved, and remains, as expected, constant in all FT-STS images, i.e. independent of the bias voltage.

To fully understand the FT-STS data, we simulated the CEC maps and their corresponding JDOS, see figure 4(b) and (c). Two closed structures are observed in the calculated CEC in the energy window where the SS extend. Then, at -600 mV, a more complex CEC arises in which the two SS bands cross forming a flower-shape pattern. Increasing the bias voltage to -500 mV, i.e. above the surface state maximum, the CEC simply reflects the shape of the bulk conical dispersion. At this particular energy, our FT-STM data shows a hexagonal-shaped intensity distribution with maxima along the $\Gamma - M$ directions due to the contribution of an independent scattering vector, q_D, between equivalent points of the CEC, see figure 4(b). Instead, JDOS calculated at -510 meV, shows a circular contour. A sixfold symmetry in these kind of systems has been attributed to a warping of the state [53–55] or an anisotropic scattering from a non-circular defect [56]. In TMDs, it was shown that the predominant defects are diffuse triangles [24, 26, 27, 31, 51, 55, 57]. In this case, the size and the shape of defects result in anisotropic waves with short wavelengths, evident from the inspection of QPI maps in figure 4(a). As a consequence, stronger signal is resolved in the FT-STS along the $\Gamma - M$ directions. These features are not captured in the JDOS, which are calculated for all possible contributions. At -600 mV, new features appear in the corresponding FT-STS image, as expected from the contribution of the scattering vectors from the SS, q_{SS}, which can be clearly resolved in the QPI map taken at -600 mV. The JDOS at this energy reproduces quite well our experimental data, in which a six-fold symmetric pattern is observed, indicating the presence of such as states. However, for larger negative bias

Figure 4. Comparison between experimental FT-STS images and JDOS. (a) Quasiparticle interference patterns of a PtTe$_2$ surface taken at different V_b (30 nm × 30 nm, I_t = 0.5 nA, V$_{mod}$ = 50 mV). Measurements were performed at 1.2 K. (b) Corresponding symmetrized Fourier transformed images partially superimposed with the simulated JDOS on the left half of the images. The white dotted hexagon indicates the spots corresponding to the atomic lattice. (c) Calculated CEC. The scale bar in (b) and (c) is the same. The scattering vector between equivalent points in the CECs for the SS, q_{SS}, and bulk Dirac cone, q_D, are indicated with arrows in (b) and (c).

voltages, −800 mV and −700 mV, the atomic lattice in PtTe$_2$ is of the same size than the wavelengths of the expected scattering vectors, q_{SS}, between equivalent points in the CECs. Consequently, the standing waves around defects present a very small wavelength, almost negligible in the QPI images. Thus, the QPI maps reflect just a reminiscence of the bulk Dirac cone states with a similar pattern that the one observed at −500 mV.

5. Conclusions

By combining STM experiments and first-principles calculations, we have studied the surface structure and electronic properties of PtTe$_2$ at the atomic scale. Our *in-situ* cleaved samples present high structural quality, as confirmed by topographic STM images. Nevertheless, we found four types of native defects. Using Tersoff–Hamann calculations, we are able to unambiguously identify the atomic nature of these defects, since each of them shows unique fingerprints in the STM simulations. Contrary to other TMDs, in our PtTe$_2$ samples the most frequent defects are related to a slight stoichiometric lack of Pt, the most common one being a single Pt vacancy in the first layer. The presence of such defects has a negligible impact on the electronic properties of the system. This is confirmed by our STS measurements, which correlate well with the calculated band structure for an ideal system. Furthermore, elastic scattering at the defects produce QPI patterns, which can be recorded in a wide range of energies, Fourier transformed and, compared with the calculated JDOS maps, allowing us to confirm the existence of the bulk Dirac cone and SS on PtTe$_2$. These results show the potential of this procedure in the characterization of the surface of novel topological semimetals.

Data availability statement

The data that support the findings of this study are available upon reasonable request from the authors.

ORCID iDs

Antonio Politano ⬤ https://orcid.org/0000-0002-4254-2102
Jose Angel Silva-Guillén ⬤ https://orcid.org/0000-0002-0483-5334
Manuela Garnica ⬤ https://orcid.org/0000-0002-7861-9490

References

[1] Kim H J, Kim K S, Wang J F, Sasaki M, Satoh N, Ohnishi A, Kitaura M, Yang M and Li L 2013 *Phys. Rev. Lett.* **111** 246603
[2] Xiong J, Kushwaha S K, Liang T, Krizan J W, Hirschberger M, Wang W, Cava R J and Ong N P 2015 *Science* **350** 413–6
[3] Feng J, Pang Y, Wu D, Wang Z, Weng H, Li J, Dai X, Fang Z, Shi Y and Lu L 2015 *Phys. Rev. B* **92** 081306
[4] Liang T, Gibson Q, Ali M N, Liu M, Cava R J and Ong N P 2015 *Nat. Mater.* **14** 280–4
[5] Liu Z K *et al* 2014 *Science* **343** 864–7
[6] Liu Z K *et al* 2014 *Nat. Mater.* **13** 677–81
[7] Borisenko S, Gibson Q, Evtushinsky D, Zabolotnyy V, Büchner B and Cava R J 2014 *Phys. Rev. Lett.* **113** 027603
[8] He L P, Hong X C, Dong J K, Pan J, Zhang Z, Zhang J and Li S Y 2014 *Phys. Rev. Lett.* **113** 246402
[9] Neupane M, Xu S Y, Sankar R, Alidoust N, Bian G, Liu C and Belopolski I 2014 *Nat. Commun.* **5** 3786
[10] Yi H *et al* 2014 *Sci. Rep.* **4** 6106
[11] Li Q, Kharzeev D E, Zhang C, Huang Y, Pletikosić I, Fedorov A V, Zhong R D, Schneeloch J A, Gu G D and Valla T 2016 *Nat. Phys.* **12** 550–4
[12] Huang H, Zhou S and Duan W 2016 *Phys. Rev. B* **94** 121117
[13] Bahramy M *et al* 2018 *Nat. Mater.* **17** 21–28
[14] Noh H J, Jeong J, Cho E J, Kim K, Min B and Park B G 2017 *Phys. Rev. Lett.* **119** 016401
[15] Deng K *et al* 2019 *Sci. Bull.* **64** 1044
[16] Yan M *et al* 2017 *Nat. Commun.* **8** 257
[17] Politano A, Chiarello G, Ghosh B, Sadhukhan K, Kuo C n, Lue C S, Pellegrini V and Agarwal A 2018 *Phys. Rev. Lett.* **121** 86804
[18] Zhang K, Yan M, Zhang H, Huang H, Arita M, Sun Z, Duan W, Wu Y and Zhou S 2017 *Phys. Rev. B* **96** 125102
[19] Ghosh B, Mondal D, Kuo C N, Lue C S, Nayak J, Fujii J, Vobornik I, Politano A and Agarwal A 2019 *Phys. Rev. B* **100** 195134
[20] Mukherjee S *et al* 2020 *Sci. Rep.* **10** 12957
[21] Fei F *et al* 2017 *Phys. Rev. B* **96** 041201
[22] Fu D *et al* 2018 *Phys. Rev. B* **97** 245109
[23] Zheng W *et al* 2018 *Phys. Rev. B* **97** 235154
[24] Wang W X *et al* 2022 arXiv:2201.00294
[25] Li J, Joseph T, Ghorbani-Asl M, Kolekar S, Krasheninnikov A V and Batzill M 2022 *Adv. Funct. Mater.* **32** 2110428
[26] Zheng H, Choi Y, Baniasadi F, Hu D, Jiao L, Park K and Tao C 2019 *2D Mater.* **6** 041005
[27] Zhussupbekov K, Ansari L, McManus J B, Zhussupbekova A, Shvets I V, Duesberg G S, Hurley P K, Gity F, Coileáin C O and McEvoy N 2021 *npj 2D Mater. Appl.* **5** 14
[28] Anemone G, Aguilar P C, Garnica M, Lue C S, Politano A, Parga A L V D and Miranda R 2021 *npj 2D Mater. Appl.* **5** 1–7
[29] Avsar A, Ciarrocchi A, Pizzochero M, Unuchek D, Yazyev O V and Kis A 2019 *Nat. Nanotechnol.* **14** 674–8
[30] Politano A, Chiarello G, Kuo C N and Lue C S 2018 *Adv. Funct. Mater.* **28** 1706504
[31] Garnica M *et al* 2022 *npj Quantum Mater.* **7** 7
[32] Simon L, Bena C, Vonau F, Cranney M and Aubel D 2011 *J. Phys. D: Appl. Phys.* **44** 464010
[33] Chen L, Cheng P and Wu K 2017 *J. Phys.: Condens. Matter* **29** 103001
[34] Anemone G *et al* 2020 *2D Mater.* **7** 025007
[35] Horcas I, Fernández R, Gómez-Rodríguez J M, Colchero J, Gómez-Herrero J and Baro A M 2007 *Rev. Sci. Instrum.* **78** 013705
[36] Giannozzi P *et al* 2009 *J. Phys.: Condens. Matter* **21** 395502
[37] Giannozzi P *et al* 2017 *J. Phys.: Condens. Matter* **29** 465901
[38] Giannozzi P *et al* 2020 *J. Chem. Phys.* **152** 154105
[39] Perdew J P, Burke K and Ernzerhof M 1996 *Phys. Rev. Lett.* **77** 3865
[40] Dal Corso A 2014 *Comput. Mater. Sci.* **95** 337–50
[41] Monkhorst H J and Pack J D 1976 *Phys. Rev. B* **13** 5188
[42] Pizzi G *et al* 2020 *J. Phys.: Condens. Matter* **32** 165902
[43] Wu Q, Zhang S, Song H F, Troyer M and Soluyanov A A 2018 *Comput. Phys. Commun.* **224** 405–16
[44] Kang S H, Jeon S, Kim H J, Ko W, Cho S, Kang S H, Kim S W, Yang H, Kim H W and Son Y W 2022 *Phys. Rev. B* **105** 045143
[45] Inoue H, Gyenis A, Wang Z, Li J, Oh S W, Jiang S, Ni N, Bernevig B A and Yazdani A 2016 *Science* **351** 1184–7
[46] Soler J M, Artacho E, Gale J D, García A, Junquera J, Ordejón P and Sánchez-Portal D 2002 *J. Phys.: Condens. Matter* **14** 2745–79
[47] García A *et al* 2020 *J. Chem. Phys.* **152** 204108
[48] Arne K and Grønvold F 1959 *Acta. Chem. Scand.* **13** 1767–74

[49] Furuseth S, Selte K, Kjekshus A, Gronowitz S, Hoffman R A and Westerdahl A 1965 Redetermined crystal structures of NiTe$_2$, PdTe$_2$, PtS$_2$, PtSe$_2$ and PtTe$_2$ *Acta Chem. Scand.* **19** 257–8

[50] Momma K and Izumi F 2011 *J. Appl. Crystallogr.* **44** 1272–6

[51] Li X *et al* 2021 *Nat. Commun.* **12** 2351

[52] Gao J, Cheng Y, Tian T, Hu X, Zeng K, Zhang G and Zhang Y W 2017 *ACS Omega* **2** 8640–8

[53] Hasan M Z and Kane C L 2010 *Rev. Mod. Phys.* **82** 3045–67

[54] Alpichshev Z, Analytis J G, Chu J H, Fisher I R, Chen Y L, Shen Z X, Fang A and Kapitulnik A 2010 *Phys. Rev. Lett.* **104** 016401

[55] Kim S *et al* 2011 *Phys. Rev. Lett.* **107** 056803

[56] Mann C 2015 arXiv:1509.07807

[57] Netsou A M, Muzychenko D A, Dausy H, Chen T, Song F, Schouteden K, Van Bael M J and Van Haesendonck C 2020 *ACS Nano* **14** 13172–9